DNS of spark-ignition in an anode-cathode configuration: impact of plasma chemical kinetics

F. Collin-Bastiani⋆ ⋆⋆⋆ †, B. Cuenot⋆, E. Riber⋆, O. Vermorel⋆, A. Cayre⋆⋆⋆,
S. Richard⋆⋆, A. Misdariis⋆ and P. Champeix⋆

⋆ CERFACS
42 Avenue Gaspard Coriolis, 31057 Toulouse, France
⋆⋆*Safran Helicopter Engines*
Avenue Joseph Szydlowski, 64511 Bordes, France
⋆⋆⋆Safran Aircraft Engines
Rond-point Rene Ravaud, 77550 Moissy-Cramayel, France

† Corresponding author Email: collin@cerfacs.fr

Abstract

Relight capabilities are a design factor for aeronautical engine manufacturers. Numerical simulation of engine ignition is a powerful tool to understand the main mechanisms driving the complex transient phases from the spark ignition to the flame stabilization on all fuel injectors of the combustion chamber. The work presented here focuses on the spark ignition phase during which a transition from a plasma to a first flame kernel occurs. Analytically Reduced Chemistries (ARCs) making the coupling between low temperature chemistry -combustion- and plasma kinetics are used in Direct Numerical Simulation (DNS) of discharge in pure air and of propane-air ignition sequences in an academic anode-cathode configuration. Results are compared to experimental data showing a good qualitative behaviour. Discrepancies on temperature evolution microseconds after the beginning of the discharge in pure air are certainly due to the energy deposition model calibration that should be improved. Taking into account the plasma chemical kinetics is found to change drastically the peak temperature because of the dissociation and ionization reactions which are endothermic. The ARC methodology appears as a promising approach to couple low and high temperature kinetics, which play a key role in the early times of ignition.

1. Introduction

In the current environmental context, major efforts are being made by the aeronautical industry to limit pollutant emissions such as NO_x, CO_2, or CO but also noise emission. These developments should always keep some crucial operability properties and capabilities of engines such as relight efficiency in case of engine failure. For example, the design of low-NO_x combustors is now widely studied but could be prejudicial to relight capabilities as it implies to work in leaner conditions. Understanding the physics of spark ignition in a two-phase flow and in flight conditions is therefore of prime interest for engine manufacturers. Spark ignition in an aeronautical engine can be divided in three main parts. The first part is the kernel formation following the electric discharge at the spark plug. The second is the growth and propagation of the flame kernel up to the nearest fuel injector and the third one is the inter-sector flame propagation. The present study focuses on the first part only. At this stage, the very small scale of the kernel allows to use Direct Numerical Simulation (DNS) to better understand the main mechanisms driving this complex transient phase.

In this first period of ignition, a spark plug delivers a very short and powerful electrical discharge to the mixture, inducing the creation of a plasma[1] and possibly combustion. To study this still poorly understood transition from the electrical discharge to a flame kernel, a suitable chemical kinetics should be used to capture both combustion and plasma chemistries. Detailed mechanisms are too costly to directly integrated in 3D DNS. One affordable solution is to use an Analytically Reduced Chemistry (ARC) including both combustion and plasma kinetics. An ARC is derived by reducing the number of reactions and transported species from a detailed mechanism using successively reduction techniques such as Directed Relation Graph (DRG) methods[2] and Quasi-Steady State Approximations (QSSA). The

final mechanism contains fewer transported species and is less stiff,[3] making it affordable for explicit integration. ARC has already been successfully used in the context of combustion in complex configurations such as the Siemens SGT-100 burner[4] or the PRECCINSTA burner.[5]

The objective of this work is to perform 3D DNS of the kernel formation following the electric discharge in a simple configuration (two facing electrodes) using the AVBP solver with an ARC coupling combustion and plasma kinetics. First, the derivation of the two ARCs (combustion only and combustion-plasma kinetics) is detailed as well as the thermodynamic and transport properties employed. The development of an appropriate ignition model needed to mimic the spark ignition phenomenology is also presented. In a second step, the chemistry description developed in this work is validated against simple test cases. Finally, DNS of the anode-cathode configuration are performed and results are confronted to experimental data. In particular, temperature fields taken few microseconds after the discharge are analysed in detailed.

2. Numerical models

2.1 Analytically reduced chemistry for combustion

An ARC dedicated to propane combustion without any plasma chemistry is derived using the YARC reduction code.[6] The chosen detailed mechanism is the iso-octane LLNL mechanism[7] made of 6,964 reactions and 874 species. During the entire reduction procedure, targeted quantities to be correctly predicted are the heat release and species mass fractions of C_3H_8, CO_2, CO, OH and O. The last two species are known to be important precursors in ignition and are thus included. Canonical applications for the reduction process are propane-air laminar flames with equivalence ratio $\phi = 0.6 - 0.8$ and 0D propane-air auto-ignition cases in the ranges $\phi = 0.6 - 1.0$ and $T = 1,100K - 1,700K$. The Directed Relation Graph method with error propagation[2] is used to discard unimportant equations and species for the selected canonical applications and targeted quantities. The Level of Importance criterion[8] is then applied to selected the best candidates to QSSA among the remaining species. The final ARC (called ARC_combu_25 later on) is made of 25 transport species, 292 reactions and 16 species in QSSA and is validated in section 3.1.

2.2 Combustion-plasma chemical kinetics description

The set of plasma chemical reactions with associated rate coefficients used (called MECH_plasma_38 hereafter) is made of 38 species and 366 irreversible reactions[9] and has already been used for plasma studies.[10] The combustion-plasma mechanism derived in this work is a simple merge of the MECH_plasma_38 and the ARC_combu_25. When redundant reactions are found, i.e. involved in both mechanisms, the reaction rate used in the ARC_combu_25 is kept. Differences between reaction rates proposed by both schemes are anyway very small. All 13 charged species of the MECH_plasma_38, known to be very reactive, are put in QSSA. The resulting merged mechanism (named MECH_merged_33 in the following) is made of 586 reactions, 30 species in QSSA and 33 transport species. Among the transported species, 12 are coming exclusively from the combustion part, 8 exclusively from the plasma contribution and 13 are common to both mechanisms. These 13 common species are essential as they bridge the gap between combustion and plasma chemistries. The MECH_merged_33 is validated in section 3.2.

2.3 Thermodynamic and transport properties

Species thermodynamic properties are taken from the NASA database.[11] Properties are available for the 63 species involved here up to $6,000\,K$ at least and $20,000\,K$ for some species. Properties are extrapolated up to $20,000\,K$ when missing. Viscosity and thermal conductivity properties of the mixture are those derived for high temperature equilibrium air plasmas by D'Angola.[12] Dissociations and recombinations occurring at high temperature are then taken into account in the transport properties temperature dependency, contrary to classical laws such as the Sutherland law.

2.4 Ignition model

The first phase of spark ignition can be divided itself in 3 main phases[1,13–15] : during breakdown $(1 - 10\,ns)$, a small amount of energy is delivered to the mixture inside a cylindrical volume between the electrodes. Even if the energy supplied is small, the energy deposition density is huge as the duration of this phase along with the volume of interest are small. Temperatures up to $20,000\,K$ or more can be reached in this inter-electrode zone leading to a intense shock wave, molecular dissociations and the creation of a radical pool. Moreover, the efficiency of this deposition is good with

less than 6 % losses by conduction to the electrodes and radiation. The arc phase ($\approx 1\,\mu s$) follows the breakdown. The energy power is at least 2 orders of magnitude lower than in the previous phase and the amount of energy delivered is small compared to the next phase. Temperatures decrease leading to recombinations and the first exothermic chemical reactions. The largest part (≈ 95 %) of the total transmitted energy during spark ignition is given during the glow phase ($\approx 1\,ms$), but with important losses mostly by conduction to the electrodes. As this phase is long, the power is again lower than in the arc phase. The mixture is cooled down so that ionization becomes negligible.

To mimic this phenomenology, the spark should be properly modelled. In particular, the spatial and temporal form of the energy deposition as well as the energy losses from electrical to thermal energy available for the mixture should be accounted for. An Energy Deposition (ED) model is used here where a volumic source term $\dot{Q}$ is added in the energy transport equation. The kernel initiation and growth are then directly solved. ED models have already been successfully used in different Direct Numerical Studies.[16] However, the temporal and spatial shapes of the source term $\dot{Q}$ were considered Gaussian and calibrated so that temperatures higher than $3000\,K$ could not be reached. More complex modelisation of the source term $\dot{Q}$ based for example on 1D modelisation of electric circuit have been derived[17] to predict accurately its temporal form.

In this work, the temporal evolution of the ED model source term $\dot{Q}$ is calculated using available experimental data of spark sequences. The form of the electrical energy $E_{elec}(t)$ as function of time is reconstructed. Then, standard efficiency coefficients are used to obtain the actual transmitted energy $E_{ign}(t)$ to the mixture after losses. Energy is considered to be deposited in two phases: the breakdown phase and the end of the discharge gathering arc and glow but called glow hereafter for simplicity. The breakdown is too short to obtain accurate experimental data but the amount of electrical energy provided during this phase E_{bd} can be estimated experimentally as well as its duration t_{bd}. Then, the simplest estimation of the electrical energy $dE_s(t)$ consumed during a small time dt is obtained by considering a constant electrical power:

$$dE_s(t) = E_{bd}\frac{dt}{t_{bd}} \tag{1}$$

The actual energy $dE_{ign}(t)$ used to ignite the mixture is then obtained by considering an efficiency coefficient $\eta = 95$ % commonly used in the literature:

$$dE_{ign}(t) = \eta\, dE_s(t) \tag{2}$$

For the second phase of energy deposition, the duration of the glow t_{glow} and the electrical energy given in this period E_{glow} are also given experimentally. $dE_s(t)$ can be reconstructed using the voltage and current signal as functions of time. It is observed that the electrical power is almost linearly decreasing. Then, with t_{spark} the end time of the spark,

$$dE_s(t) = \frac{2\,E_{glow}\,dt}{t_{glow}{}^2}(t_{spark} - t). \tag{3}$$

Applying an efficiency coefficient $\zeta = 30$ % also found in the literature gives

$$dE_{ign}(t) = \zeta\, dE_s(t) \tag{4}$$

for the glow phase. Finally, the energy deposition volume is approximated to a cylinder between the two electrodes as represented in Fig.1. Its length is fixed to $l_{cyl} = 2.4\,mm$ and its diameter is d_{cyl}. A hyperbolic tangent function is used to smooth the deposition around this cylinder.

3. Validation of the chemical kinetics

3.1 Validation of the ARC_combu_25 and MECH_plasma_38 schemes

The ARC_combu_25 scheme is validated in the range of flame temperatures i.e. under $3,000\,K$. It is compared to the detailed LLNL mechanism in terms of laminar unstrained premixed flame at 1 bar and 298 K in Fig. 2. Experimental data from Jomaas et al.[18] and Vagelopoulos et al.[19] are also reported showing the accuracy of the ARC. The agreement between the detailed mechanism and the ARC is very good with less than 5 % relative error for equivalence ratios in the range $0.6 < \phi < 1.4$. Auto-ignition delay times at 1 bar and $\phi = 1$ as function of the temperature are also well recovered by the ARC_combu_25 as shown by Fig.3 with relative errors being under 15 % for temperatures $1,100\,K <$
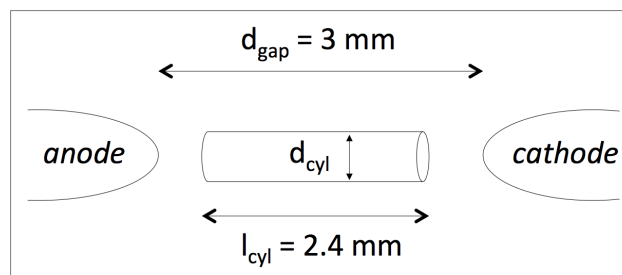
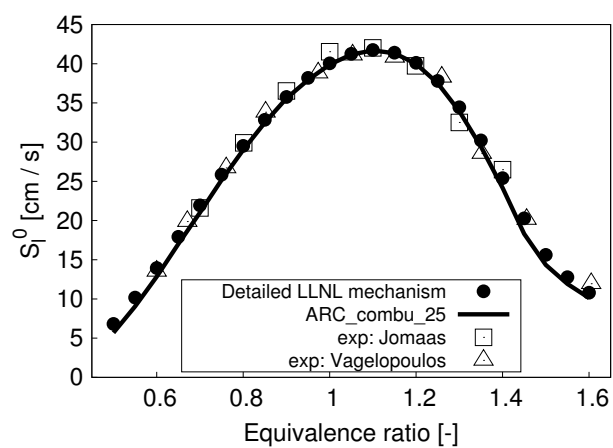Figure 1: Cylindrical volume of energy deposition in the numerical model.

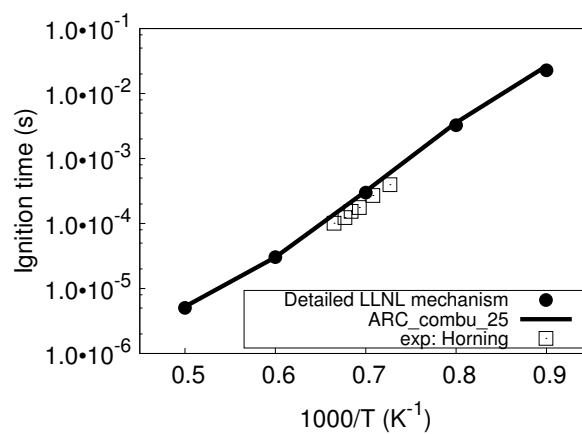Figure 2: Laminar unstrained premixed flame at 1 bar and 298 K

Figure 3: Auto-ignition delay time at 1 bar and $\phi = 1$ as function of the temperature

Table 1: Relative errors on the final temperature T_{final} and species molar fractions X^i_{final} obtained starting from different temperatures T_{ini}

T_{ini} (K)	3,000	5,000	7,000	15,000	20,000
ε_T	0.00051	-0.00032	0.00148	-0.0109	-0.0071
ε_X	0.0023	0.0093	0.029	0.047	0.021

Table 2: Relative errors on the final species molar fractions X^i_{final} obtained starting from different temperatures T_{ini} K

$T_{ini} - T_{final}$(K)	20,000-15,000	15,000-20,000	10,000-3,000	3,000-10,000
ε_X	0.094	0.082	0.009	0.086

$T < 2,000\,K$. Both the detailed mechanism and the ARC_combu_25 are in good agrement with experimental data from Horning et al.[20]

The MECH_plasma_38 scheme must be correct at temperatures where ionization and dissociation reactions take place so for $T > 3,000\,K$. Due to the lack of data on kinetics, only thermodynamic validations are done here. The software Cantera[21] is used as well as the NASA Chemical Equilibrium with Applications (CEA) code.[22] In the first test case, a constant pressure reactor is simulated starting at an arbitrary initial temperature T_{ini} and with the equilibrium composition $X_{eq}(T_{ini})$ at T_{ini} given by the CEA code. The initial molar fraction X^i_{ini} of species i is then $X^i_{ini} = X^i_{eq}(T_{ini})$. Table 1 shows the relative errors ε_T and ε_X on the final temperature T_{final} and final species molar fraction X^i_{final} starting from different temperatures T_{ini}. ε_T and ε_X are defined in Eq. 5 and 6.

$$\varepsilon_T = \frac{T_{final} - T_{ini}}{T_{ini}} \tag{5}$$

$$\varepsilon_X = \frac{1}{N_{spec}} \sum_i \frac{X^i_{final} - X^i_{ini}}{X^i_{ini}} \tag{6}$$

The temperature remains close to T_{ini} with less than 1 % relative error and the composition also stays close to the equilibrium composition at T_{ini} with errors under 5 %. The electro-neutrality is preserved as well. In the second test case, a constant pressure reactor is simulated also starting at an arbitrary initial temperature T_{ini} and with the equilibrium composition $X_{eq}(T_{ini})$ at T_{ini}. But here the final temperature T_{final} is imposed different from T_{ini}. The final composition of the mixture is expected to be equal to the equilibrium composition of the mixture at T_{final} given by the CEA code. The relative error ε_X on the composition, given in Eq. 7, is computed for different couples T_{ini}-T_{final} in Tab. 2.

$$\varepsilon_X = \frac{1}{N_{spec}} \sum_i \frac{X^i_{final} - X^i_{eq}(T_{final})}{X^i_{eq}(T_{final})} \tag{7}$$

Even with important temperature and composition differences, species molar fractions are still well recovered. For example, taking the couple $T_{ini} - T_{final} = 10,000\,K - 3,000\,K$, the molar fraction of almost all species undergoes a huge variation due to recombination reactions. The molar fraction of species OH goes from 4e-6 to 3e-2 for instance. Nevertheless, the final composition of the mixture is recovered with a deviation from equilibrium of only 1 %. Finally a last test case has been performed showing that starting at T_{ini} and with a composition different from the equilibrium composition at T_{ini}, an equilibrium state is recovered with good precision as long as the initial departure from equilibrium composition is not too big. This last point is key to ensure the robustness of the chemical system in case of acceptable departure from equilibrium during calculation.

3.2 Validation of the MECH_merged_33 mechanism

Four conditions are required for the MECH_merged_33 to be accurate. Under $3,000\,K$, the combustion part of the mechanism should be precise and the plasma part should be totally inactive as it is irrelevant at such temperatures. On the contrary, for $T > 3,000\,K$, the plasma part should be accurate and the combustion contribution should be negligible. The "de-connexion" of the irrelevant part of the mechanism in both low and high temperatures is not forced but expected correct by construction. For $T < 3,000\,K$, it is compared to the detailed LLNL mechanism and the
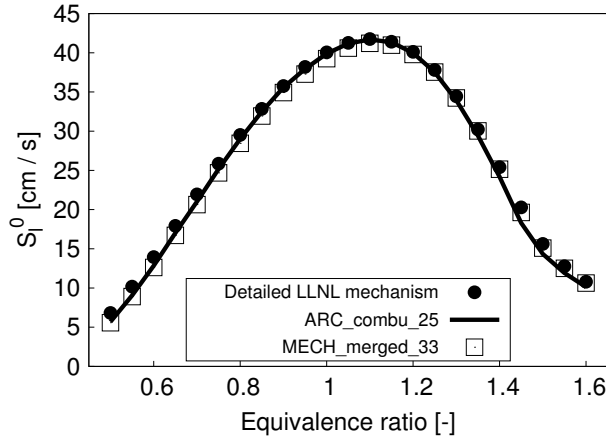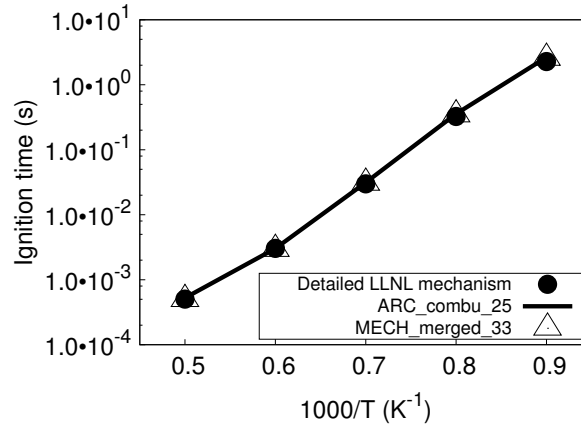
Figure 4: Laminar unstrained premixed flame at 1 bar and 298 K

Figure 5: Auto-ignition delay time at 1 bar and $\phi = 1$ as function of the temperature

ARC_combu_25 for both laminar unstrained premixed flame at 1 bar and 298 K and auto-ignition delay time at 1 bar and $\phi = 1$ in Figs. 4 and 5. No difference is observed with the ARC_combu_25 showing that, as expected, the plasma part of the mechanism is inactive at low temperature.

A test case is also performed to validate the MECH_merged_33 at high temperatures. A constant pressure reactor is simulated starting with a stoichiometric $C_3H_8 - air$ mixture at $T_{ini} = 300\,K$. The final temperature is imposed at $T_{final} = 10,000\,K$. The final composition of the mixture is expected to be equal to the equilibrium composition of the mixture at T_{final} given by the CEA code. This validation case is important as a transition from combustion to plasma temperatures occurs. The relative errors ε_X^i on the remaining transported species final molar fraction, given in Eq. 8, are given in Tab. 3.

$$\varepsilon_X^i = \frac{X_{final}^i - X_{eq}^i(T_{final})}{X_{eq}^i(T_{final})} \tag{8}$$

An overall good agreement is obtained for the major remaining species molar fractions. The mean relative error is 7 % with a maximum relative discrepancy of 17 % for the atomic carbon molar fraction. These relative errors are acceptable

Table 3: Relative errors ε_X^i on the remaining transported species final molar fraction starting with a stoichiometric $C_3H_8 - air$ mixture at $T_{ini} = 300\,K$

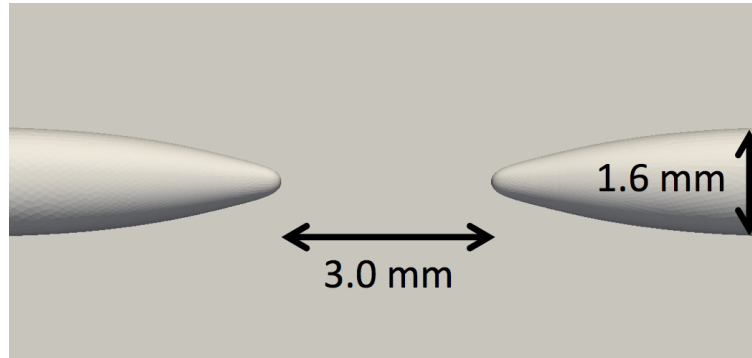| species	C	N	O	H
ε_X^i	0.17	0.07	0.015	0.037

Figure 6: Sketch of the electrodes shape.

for the targeted application of this work.

The merge of the combustion and plasma chemistries in the MECH_merged_33 has been demonstrated correct and efficient in this section. As expected, each part is inactive in temperature ranges where it is irrelevant. The MECH_merged_33 is now used in DNS of an anode-cathode configuration.

4. Application to an anode-cathode configuration

4.1 Configuration description and Numerical set-up

The configuration studied here is an academic set-up experimented at CORIA laboratory (Rouen, France). It is made of two facing 2.2 cm long shaped electrodes as illustrated in Fig. 6. The maximal diameter of the electrodes is 1.6 mm and the electrode gap $d_{gap} = 3\,mm$. The numerical domain is reduced to 1/8 of a sphere as sketched in Fig.7. Its radius is 10 cm and its center is the middle point between the two electrodes so that the head of the electrodes is at $[x = \pm1.5\,mm, y = 0.0\,mm, z = 0.0\,mm]$. This domain reduction assumes that (xy,yz,zx)-planes are symmetry planes. This assumption is verified for planes xy and zx but a temperature gradient is experimentally observed between the two electrode heads during spark so that the yz-plane is not a symmetry plane. However, for simplicity, no such gradient is considered in the energy deposition model and the yz-plane is kept as a plane of symmetry. Symmetry conditions are then applied on faces 1, 2 and 3 of the domain as shown in Fig. 7. A NSCBC condition[23] is employed for the outlet face 4, fixing pressure to 1 bar. Finally, a no-slip adiabatic condition is used on the electrode walls. Indeed, no losses are directly computed at the walls as they are already accounted for by the η and ζ factors applied to the actual transmitted energy, see Eqs.2 and 4.

Concerning the general numerical set-up, the third-order explicit TTGC centered scheme[24] is used. The first $2\,\mu s$ of physical time are always simulated on a 2.1 million tetrahedral cells mesh with a characteristic grid size in the inter-electrodes gap of 15 microns. Such a small grid size is required during the breakdown phase in the energy deposition zone to resolve the strong gradients and chemical source terms. After $2\,\mu s$, the solution is interpolated and the calculation continues on a coarser 1.0 million cells mesh with the smallest grid size being of the order of 50 microns. The time step is constrained by convection/diffusion processes via a CFL number but also by the chemical system. Time steps range from $0.03\,ns$ to $0.5\,ns$ during the first $2\,\mu s$ of physical time and up to $1\,ns$ after $2\,\mu s$. Chemistry sub-cycling is also used for the first $2\,\mu s$ of physical time to improve the stability of the explicit time integration.

4.2 Numerical investigations

Before simulating propane-air ignition sequences, discharges in air are first investigated to understand the impact of plasma reactions on the O_2-N_2 mixture dynamics. The electrical signals $E_{elec}(t)$ are used to reconstruct the model inputs for both propane-air and pure air cases. All energy deposition model parameters are gathered in Tab. 4. The indicated energies in this table are divided by 8 as our numerical domain is only 1/8 of the 3D sphere. The breakdown time t_{bd} is fixed to $20\,ns$ as more accurate experimental measurements of this duration are too difficult to obtain. The diameter of the energy deposition cylinder is 130 microns for the discharge in air. For the propane-air ignition, this diameter is increased up to 200 microns to smooth gradients that are stronger in this case than in pure air.

For the case of discharge in pure air, two computations are performed. Both are initialized with an inert air mixture (N_2-O_2) at atmospheric conditions. In the first case, no plasma reactions are considered so that the entire deposited energy is used for thermal heating of the mixture. In the second case, plasma chemistry is activated with the MECH_merged_33.
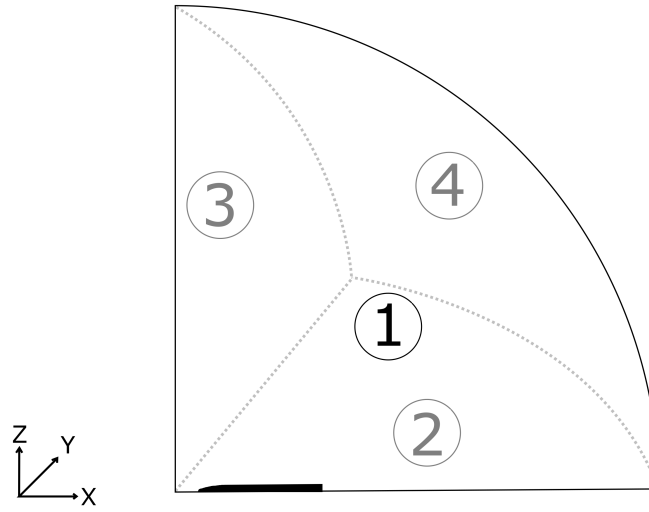
Figure 7: Scaled representation of the numerical domain.

Table 4: Energy deposition model inputs for the case of discharge in air.

Case	E_{bd}	t_{bd}	E_{glow}	t_{glow}	d_{cyl}
Discharge in air	2.8 mJ	20 ns	77 mJ	2.7 ms	130 μm
Propane-air ($\phi = 1$) ignition	5.0 mJ	20 ns	110 mJ	4.0 ms	200 μm

Then, the energy deposited by the ignition model is used partly for heating but also to trigger dissociation and ionisation reactions. In this last case, radial cuts of temperature and pressure fields at 4 moments after the beginning of the discharged are displayed respectively in Fig.8 and Fig.9. The first two snapshots of Fig.8 give an idea of the spatial energy deposition shape. The hot gas expansion is first controlled by the shock wave until around $1\,\mu s$ and then by thermal diffusion only, the shock wave propagating faster as evidenced in the 4th image of Fig.9. At $2\,\mu s$, a depression following the shock wave is observed between the two electrodes. This depression leads to an inward gaseous flow near the spark gap and finally to a pair of counter-rotating vortices as already shown by Kono et al.[25]

The evolution of the temperature at the center of the energy deposition zone versus time with and without the plasma set of reactions is displayed in Fig. 10. Without considering any reaction, the total energy given to the mixture is used for heating so that the temperature reaches almost $15,000\,K$ at the end of the breakdown phase. With all plasma reactions activated, the maximum temperature reached after $20\,ns$ is much smaller, around $10,000\,K$. This is explained by dissociation and ionization reactions (transforming O_2 and N_2 molecules into atomic oxygen and nitrogen and again into O^+ and N^+) which are endothermic. A part of the energy delivered in the breakdown phase is then
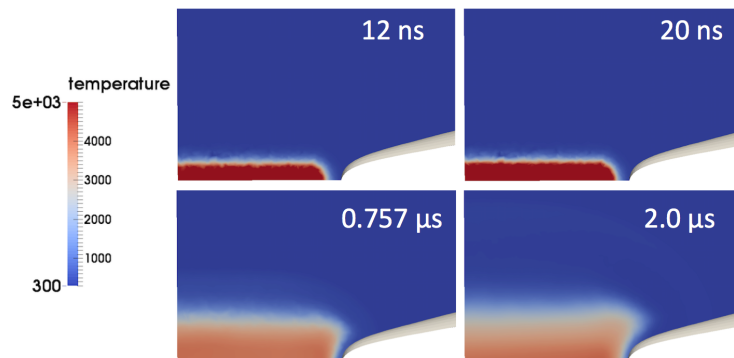

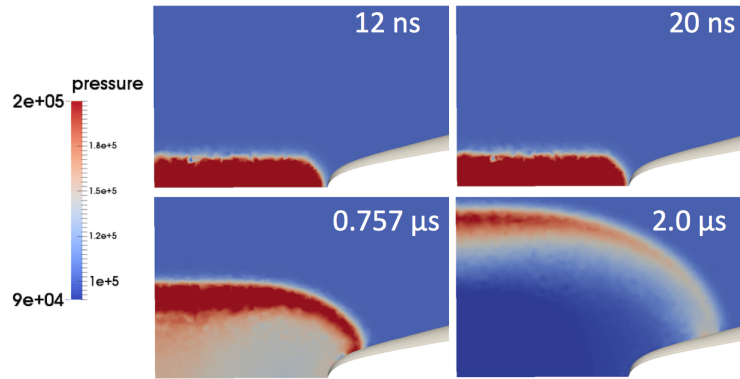Figure 8: Temperature fields at 4 moments shortly after the discharge start, with the MECH_merged_33.

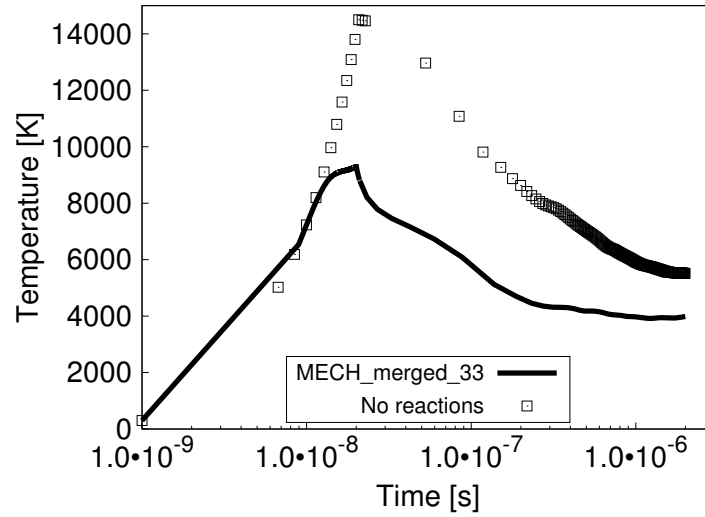Figure 9: Pressure fields at 4 moments of the discharge, using the MECH_merged_33.

Figure 10: Evolution of the temperature at the center of the two electrodes versus time using the plasma set of reactions (MECH_merged_33) or no reactions.

converted in chemical energy and kept in the chemical system until exothermic recombination reactions occur when the temperature decreases enough. After $2\,\mu s$, the temperature obtained without plasma chemistry is $5,500\,K$. This temperature decrease is only driven by diffusion effects. With plasma reactions, the temperature drops from around $10,000\,K$ down to $4,000\,K$. The temperature difference between the two cases is then considerably reduced after some microseconds as exothermic reactions in the MECH_merged_33 are activated and compensate the cooling by diffusion effects.

Tens of microseconds after the discharge start, thermal diffusion effects are overcome by the convective flow motion induced by the counter-rotating vortices. Fresh gases are coming inward along the electrodes, heat in the middle region and leave the inter-electrode gap with a radial velocity. This results in the separation of a hot gases torr from the hot central core as illustrated by Fig.11. Temperature profiles at different heights are compared to experimental data in Fig.12 $200\,\mu s$ after the discharge start. It is observed that temperatures obtained numerically are too high in the center at both $750\,\mu m$ and $1,250\,\mu m$ above the central line. This may be explained by the value of d_{cyl}, the diameter of the cylinder where the energy is deposited. Experimentally, no measurement of the plasma volume dimensions created during discharge is available. This parameter is however crucial in numerical simulations. If this diameter is too high, the induced central hot gases pocket is too large after few microseconds. After tens of microseconds, the fluid radial convection presented in Fig.11 entrains a part of the too large hot gases kernel, explaining the higher temperature observed at $750\,\mu m$ and $1,250\,\mu m$ above the central line. Reducing d_{cyl} too much would however increase the energy deposition density and the peak temperature at the center leading to numerical stability issues as well as difficulties to define thermodynamic and transport properties of species at such high temperature. Energy deposition efficiency parameters η and ζ are also parameters very difficult to estimate experimentally and play a similar role.
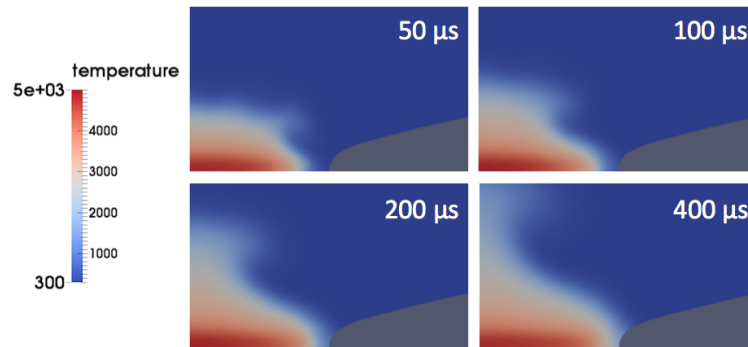
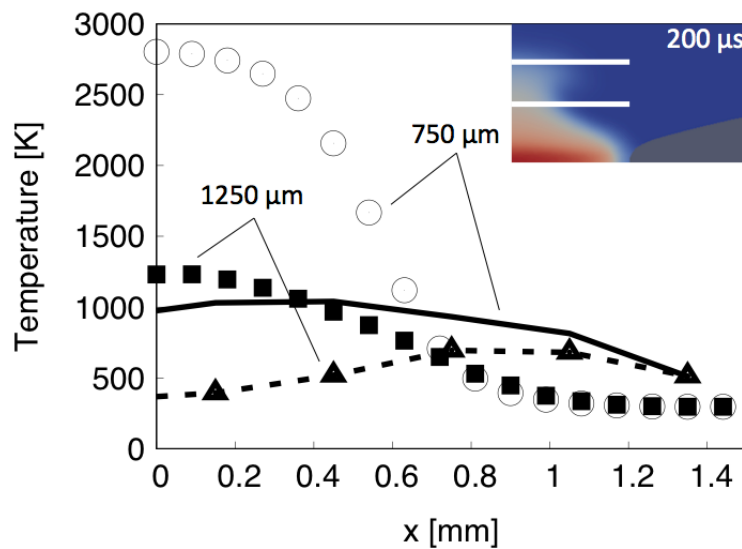Figure 11: Temperature fields at 4 moments after the discharge start, with the MECH_merged_33.

Figure 12: Temperature profiles at 2 different heights (represented by white lines on the top right corner sketch of the configuration) at $200\,\mu s$. Lines are for experimental data, Symbols are for results obtained with the MECH_merged_33.

A reactive case, starting initially with a stoichiometric propane-air mixture at rest, is now simulated with the MECH_merged_33 mechanism considering the energy deposition model inputs detailed in Tab.4. The temperature field obtained after $2\,\mu s$ is shown in Fig.13. Temperatures are relatively low, no temperature above $5,000\,K$ is found even at the end of break-down. As previously mentioned, this is explained by the parameter d_{cyl} that is increased from 130 microns in the pure air case to 200 microns in this reactive case because of stability issues. As a consequence, the peak temperature is lower and only few plasma reactions are triggered. However, the phenomenology of ignition is correctly recovered using this mechanism showing the good coupling between combustion and plasma. A calibration of the ignition model to reach higher temperature and trigger more plasma reactions should be done for the coming calculations.

5. Conclusions and perspectives

Two ARCs, one for combustion only and one combining combustion and plasma chemistries, as well as the associated thermodynamic and transport properties have been derived. Validations included 1D flame propagation speeds, auto-ignition delay times for the combustion and thermodynamic equilibrium composition for the plasma. An appropriate ignition model that mimics the spark ignition phenomenology has also been developed. DNS of propane-air ignition and discharge in air in the anode-cathode configuration were performed using the developed ignition model and chemistry description. They are compared to experimental data showing some discrepancies on temperature fields few microseconds after the discharge start. Theses differences may be due to numerical parameters such as the diameter of the energy deposition cylindrical volume that should be better calibrated to mimic the shape of the energy delivered by a spark plug both in time and space. The impact of the plasma kinetic scheme is clearly demonstrated in the case of the discharge in air. Temperature at the center of the two electrodes reaches much higher values when ignoring plasma re-

Figure 13: Temperature fields $2\,\mu s$ after the ignition beginning, starting with a stoichiometric propane-air mixture, and using the MECH_merged_33.

actions as those include endothermic dissociation and ionization reactions. The mechanism combining combustion and plasma kinetics has been successfully used in a propane-air ignition sequence demonstrating its ability to describe the transition from plasma to combustion. This chemistry description methodology is therefore promising in the context of spark ignition and this study will be continued with a better calibration of the energy deposition model.

6. Acknowledgements

References

[1] Rudolf Maly and Manfred Vogel. Initiation and propagation of flame fronts in lean ch 4-air mixtures by the three modes of the ignition spark. In *Symposium (International) on Combustion*, volume 17, pages 821–831. Elsevier, 1979.

[2] Perrine Pepiot-Desjardins and Heinz Pitsch. An efficient error-propagation-based reduction method for large chemical kinetic mechanisms. *Combustion and Flame*, 154(1):67–81, 2008.

[3] Tianfeng Lu, Chung K Law, Chun Sang Yoo, and Jacqueline H Chen. Dynamic stiffness removal for direct numerical simulations. *Combustion and Flame*, 156(8):1542–1551, 2009.

[4] T Jaravel, E Riber, B Cuenot, and G Bulat. Large eddy simulation of an industrial gas turbine combustor using reduced chemistry with accurate pollutant prediction. *Proceedings of the Combustion Institute*, 36(3):3817–3825, 2017.

[5] Benedetta Franzelli, Eleonore Riber, and Bénédicte Cuenot. Impact of the chemical description on a large eddy simulation of a lean partially premixed swirled flame. *Comptes Rendus Mécanique*, 341(1-2):247–256, 2013.

[6] Perrine Pepiot. *Automatic strategies to model transportation fuel surrogates*. PhD thesis, Stanford University, 2008.

[7] Henry J Curran, Paolo Gaffuri, William J Pitz, and Charles K Westbrook. A comprehensive modeling study of iso-octane oxidation. *Combustion and flame*, 129(3):253–280, 2002.

[8] T Løvs, D Nilsson, and F Mauss. Automatic reduction procedure for chemical mechanisms applied to premixed methane/air flames. *Proceedings of the Combustion Institute*, 28(2):1809–1815, 2000.

[9] Ph Teulet, JJ Gonzalez, A Mercado-Cabrera, Y Cressault, and A Gleizes. One-dimensional hydro-kinetic modelling of the decaying arc in air–pa66–copper mixtures: I. chemical kinetics, thermodynamics, transport and radiative properties. *Journal of Physics D: Applied Physics*, 42(17):175201, 2009.

[10] Ph Teulet, JJ Gonzalez, A Mercado-Cabrera, Y Cressault, and A Gleizes. One-dimensional hydro-kinetic modelling of the decaying arc in air–pa66–copper mixtures: Ii. study of the interruption ability. *Journal of Physics D: Applied Physics*, 42(18):185207, 2009.

[11] Bonnie J McBride, Sanford Gordon, and Martin A Reno. Coefficients for calculating thermodynamic and transport properties of individual species. 1993.

[12] Antonio D'angola, Gianpiero Colonna, C Gorse, and M Capitelli. Thermodynamic and transport properties in equilibrium air plasmas in a wide pressure and temperature range. *The European Physical Journal D-Atomic, Molecular, Optical and Plasma Physics*, 46(1):129–150, 2008.

[13] S Refael and E Sher. A theoretical study of the ignition of a reactive medium by means of an electrical discharge. *Combustion and flame*, 59(1):17–30, 1985.

[14] MT Lim, RW Anderson, and Vedat S Arpaci. Prediction of spark kernel development in constant volume combustion. *Combustion and flame*, 69(3):303–316, 1987.

[15] E Sher, J Ben-Ya'ish, and T Kravchik. On the birth of spark channels. *Combustion and flame*, 89(2):186–194, 1992.

[16] N Chakraborty, E Mastorakos, and RS Cant. Effects of turbulence on spark ignition in inhomogeneous mixtures: a direct numerical simulation (dns) study. *Combustion science and technology*, 179(1-2):293–317, 2007.

[17] O Colin and K Truffin. A spark ignition model for large eddy simulation based on an fsd transport equation (issim-les). *Proceedings of the Combustion Institute*, 33(2):3097–3104, 2011.

[18] Grunde Jomaas, XL Zheng, DL Zhu, and CK Law. Experimental determination of counterflow ignition temperatures and laminar flame speeds of c 2–c 3 hydrocarbons at atmospheric and elevated pressures. *Proceedings of the Combustion Institute*, 30(1):193–200, 2005.

[19] Christine M Vagelopoulos and Fokion N Egolfopoulos. Direct experimental determination of laminar flame speeds. In *Symposium (international) on combustion*, volume 27, pages 513–519. Elsevier, 1998.

[20] David Charles Horning, DF Davidson, and RK Hanson. Study of the high-temperature autoignition of n-alkane/o/ar mixtures. *Journal of Propulsion and Power*, 18(2):363–371, 2002.

[21] David G. Goodwin, Harry K. Moffat, and Raymond L. Speth. Cantera: An object-oriented software toolkit for chemical kinetics, thermodynamics, and transport processes, 2017. Version 2.3.0.

[22] Bonnie J McBride and Sanford Gordon. Computer program for calculation of complex chemical equilibrium compositions and applications ii. users manual and program description. 2; users manual and program description. 1996.

[23] Thierry Poinsot and SK Lele. Boundary conditions for direct simulations of compressible viscous flows. *Journal of computational physics*, 101(1):104–129, 1992.

[24] Olivier Colin and Michael Rudgyard. Development of high-order taylor–galerkin schemes for les. *Journal of Computational Physics*, 162(2):338–371, 2000.

[25] M Kono, K Niu, T Tsukamoto, and Y Ujiie. Mechanism of flame kernel formation produced by short duration sparks. In *Symposium (International) on Combustion*, volume 22, pages 1643–1649. Elsevier, 1989.